*Electronic supplementary information*

# Synergistic Electronic Modulation of Ru Sites via N-Doped $CeO_2$ and Cs Promotion for High Efficiency $H_2$ Generationfrom Ammonia Decomposition

Thien An Le [a,1], Youngmin Kim [a,1], Seung Ju Han [a,b], Younghwan Im [a], Min Sik Kim [a], You-Jin Lee [a], Ho-Jeong Chae [a*]

[a] *Chemical Process Research Division, Korea Research Institute of Chemical Technology, 141 Gajeong-ro, Yuseong-gu, Daejeon 34114, South Korea*

[b] *Department of Advanced Materials and Chemical Engineering, University of Science and Technology (UST), Daejeon 34113, South Korea*

[1] These authors contributed equally to this work

*E-mail: hjchae@krict.re.kr

* To whom all correspondence should be addressed

# Experimental

## Preparation of catalysts

N-doped $CeO_2$ supports with different N amounts were synthesized by thermal pyrolysis of urea in a nitrogen atmosphere at 500 $^oC$. Briefly, 1.0 g of $CeO_2$ (US3136, 99.97%, 50 nm) was mixed with urea powder (Sigma-Aldrich, min. 99%) at various weight ratios (urea/$CeO_2$ = 1.0, 2.0, and 3.0) and then placed inside a horizontal tubular quartz reactor on a ceramic boat. The pyrolysis process was conducted using a temperature-controlled electric furnace, with an inert $N_2$ gas flow (50 mL/min) introduced into the reactor at 500 °C. The reactor temperature was raised at 4°C/min and maintained at the target temperature for 5 h before being cooled to room temperature under the same $N_2$ gas flow. The prepared support materials were designated as 1N-$CeO_2$, 2N-$CeO_2$, and 3N-$CeO_2$, corresponding to the urea-to-$CeO_2$ ratios.

The 2 wt% Ru-based catalysts were synthesized via solvothermal synthesis. First, 1.0 g of $CeO_2$ or N-doped $CeO_2$ support described above was suspended in a mixture of 30 mL of D.I. water and 30 mL of Ethylene Glycol (99.5%, Samchun). The suspension was stirred for 30 minutes, then 1.27 mL of $Ru(NO)(NO_3)_x(OH)_y$ (Sigma-Aldrich, Ru, 1.5%) was added and stirred for a further 30 minutes. Then, the mixture was transferred to an autoclave for convection drying at 160 °C for 8 h. After cooling to room temperature, the precipitate was collected by filtration and washed thoroughly with hot D.I. water and ethanol several times before vacuum drying at 110 $^oC$ for 12 h.

## Characterization

Ru loading was quantified by inductively coupled plasma mass spectroscopy (ICP-MS) using an Agilent 720 spectrometer. For $N_2$ physisorption studies, a Micromeritics ASAP 2020 system was employed. Before analysis, the catalyst samples were vacuum degassed at 110°C for 6 h to remove adsorbed contaminants. Specific surface areas were measured using the Brunauer–Emmett–Teller ($S_{BET}$) model. Bulk crystallinity was assessed by X-ray diffraction (XRD) on a Rigaku D/Max instrument equipped with Cu Kα radiation (λ = 1.5406 Å), operating at 40 kV/40 mA. Surface chemical states were probed using X-ray photoelectron spectroscopy (XPS) on a Thermo Fisher Scientific Sigma Probe system with Al Kα excitation (1486.6 eV). Charge correction referenced adventitious carbon (C 1s at 284.8 eV). Synchrotron-based X-ray absorption spectroscopy (XAS) at the Ru K-edge (22,117 eV) was studied by the 7D beamline

of the Pohang Accelerator Laboratory (PLS-II, 3.0 GeV), utilizing a Si(111) double-crystal monochromator. XANES and EXAFS data were collected in fluorescence mode and processed using Athena and Artemis software.

Morphology features were observed by transmission electron microscopy (TEM) and high-angle annular dark-field scanning TEM (HAADF-STEM), with corresponding energy-dispersive X-ray spectroscopy (EDS) mapping, on a FEI Titan G2 microscope operated at 300 kV. Defect characterization was studied by Raman spectroscopy (Horiba LabRAM HR Evolution, at 514 nm from Argon ion laser, 1 $cm^{-1}$ resolution) and electron paramagnetic resonance (EPR) spectroscopy (Bruker A300, X-band frequency 9.64 GHz, ambient temperature).

Ru dispersion measurements employed pulsed CO chemisorption (BELCAT-II) using a modified $O_2$-$CO_2$-$H_2$-CO titration protocol to minimize spillover.[1] Reducibility was probed through hydrogen temperature-programmed reduction ($H_2$-TPR) in 9.99% $H_2$/Ar (50 mL/min, 50–900 °C ramp). Acidity and basicity were determined via $NH_3$ and $CO_2$ temperature-programmed desorption (TPD) on a BELCAT-II system, respectively: samples were pretreated in He at 110 °C (1 h), cooled to 35 °C, saturated with probe gas (9.99% $NH_3$/He or pure $CO_2$), purged, then heated to 900 °C (10 °C/min) under the He flow. $N_2$-TPD followed similar protocols using 99.99% $N_2$ adsorption at 100 °C for 1 h after in-situ $H_2$ reduction (500 °C, 2 h). $NH_3$-TPSR was conducted over reduced catalysts with a calculated 5% $NH_3$/He volume, corresponding to a mass of the loaded sample adjusted to achieve a WHSV of 6,000 $mL_{NH3}/g_{cat.}/h$. The TPSR and TPD profiles were monitored by mass and thermal conductivity detectors.

**DFT Calculation**

Density functional theory (DFT) calculations were performed using the Vienna Ab Initio Simulation Package (VASP).[2, 3] In the computations, the Bayesian error estimation functional with van der Waals correlation (vdW-BEEF) was employed within the generalized gradient approximation (GGA).[4] During the calculation, a kinetic cutoff energy of 450 eV was applied. The stopping criteria for the electronic and geometric steps were set to $10^{-2}$ eV and $10^{-4}$ eV, respectively. A 2 × 2 × 1 gamma-centered k-point mesh grid optimized surface structure. The bottom layer was fixed during relaxation in the surface slab model, and a 10 Å vacuum was applied. The formation energy ($\Delta E^{int}$) and free formation energy ($\Delta G^{int}$) were defined as

follows.[5]

$$\Delta E_{Nx*}^{int} = E(n_N = x) - E_{slab} -- n_N E_{N_2}/2 \quad (1)$$

$$\Delta G_{Nx*}^{int} = \Delta E_{Nx*}^{int} + \Delta ZPE - T\Delta S \quad (2)$$

where $E(n_N = x)$ is the electronic energy of the slab with the adsorbate and $E_{slab}$ is the energy of the slab.

The ideal gas assumption and harmonic limit approximation were applied to the gas and adsorbate, respectively. To accurately evaluate formation energies with the vdW-BEEF functional, the electronic energies of $N_2$ (g) were corrected as in the previous literature.[6, 7]

The oxygen vacancy forming energy of the $CeO_2$ surface $E_{f,n}$ was calculated as follows:

$$E_{vac} = E_{CeO_{2-}vac} + \left(G_{H_2O} - G_{H_2}\right) - E_{CeO_2} \quad (3)$$

where $E_{CeO_{2-}vac}$ is the electronic energy of the $CeO_2$ surface containing one oxygen vacancy, and $E_{CeO_2}$ is the electronic energy of the pristine $CeO_2$ surface. The Gibbs free energy of oxygen ($G_O$) was estimated from those of water ($G_{H_2O}$) and hydrogen ($G_{H_2}$).

**Catalytic Activity Evaluation**

The catalytic decomposition of $NH_3$ was systematically investigated in a fixed-bed flow reactor under ambient pressure. A quartz tubular reactor (7 mm internal diameter) was loaded with 100 mg of catalyst sieved to 45–80 mesh. Before the reaction, the catalyst was in situ reduced under a flow of 30 mL/min pure $H_2$ at 500 °C (with a 4 °C/min ramp rate) for 2 h. Residual $H_2$ was removed with pure Ar (30 mL/min) for 1 h before cooling to the reaction setup temperatures. Then, $NH_3$ (anhydrous, 99.99%) was introduced at 10 mL/min, yielding a weight hourly space velocity (WHSV) of 6,000 $mL_{NH3}/g_{cat.}/h$. WHSV was incrementally increased to 30,000 $mL_{NH3}/g_{cat.}/h$ by adjusting the $NH_3$ flow rate (50 mL/min). Temperature-dependent activity was assessed by stepwise heating from 350 °C to 450 °C in 50 °C increments, with around 30 minutes of stabilization at each temperature to ensure steady-state operation. The exit stream was analyzed using a gas chromatograph (YL Instrument 6500GC) equipped with a Porapak-N and a MoleSieve 13X column, both connected to a thermal conductivity detector (TCD).

Catalytic performance was quantified by calculating the $NH_3$ conversion ($X_{NH_3}$), $H_2$ formation rate ($r_{H_2}$), and turnover frequency ($TOF$):

$$X_{NH_3}(\%) = \frac{[NH_3]_{in} - [NH_3]_{out}}{[NH_3]_{in}} \times 100 \quad (4)$$

$$r_{H_2}\left(mmol/g_{cat.}/\,min\right) = \frac{\frac{V_{NH_3}}{22.4}.X_{NH_3}.1.5}{m_{cat.}} \quad (5)$$

$$TOF\ (s^{-1}) = \frac{r_{H_2}.M_{Ru}}{D_{Ru}.\%Ru} \quad (6)$$

$[NH_3]_{in}$ / $[NH_3]_{out}$ - $NH_3$ concentration in the feed stream/exit stream (*mol/mL*); $V_{NH_3}$- $NH_3$ flow rate (*mL/min*); $m_{cat.}$- catalyst mass (*g*); $M_{Ru}$- Ru molecular weight (*g/mol*); $D_{Ru}$- Ru dispersion (*%*); $\%Ru$- Ru percentage (*%*)

The apparent activation energy ($E_a$) of Ru-based catalysts was calculated by the Arrhenius equation below after collecting data at low $NH_3$ conversion (less than 20%).

$$k = Aexp(\frac{-E_a}{RT}) \quad (7)$$

$k$ - the reaction rate constant; $A$ - the frequency factor; $R$ - the gas constant; $T$ - the absolute temperature.

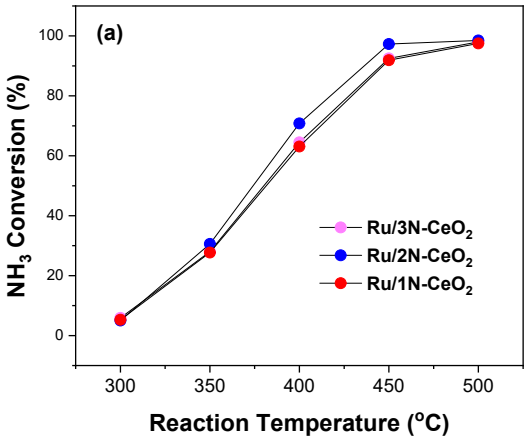


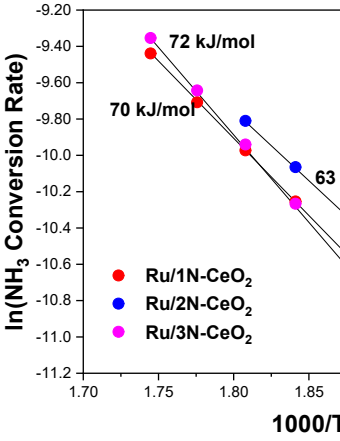


**Fig. S1.** (a) Catalytic activity of Ru-supported catalysts with different N-$CeO_2$ supports at WHSV = 6,000 $mL_{NH3}/g_{cat.}/h$ and (b) corresponding $E_a$ plots.

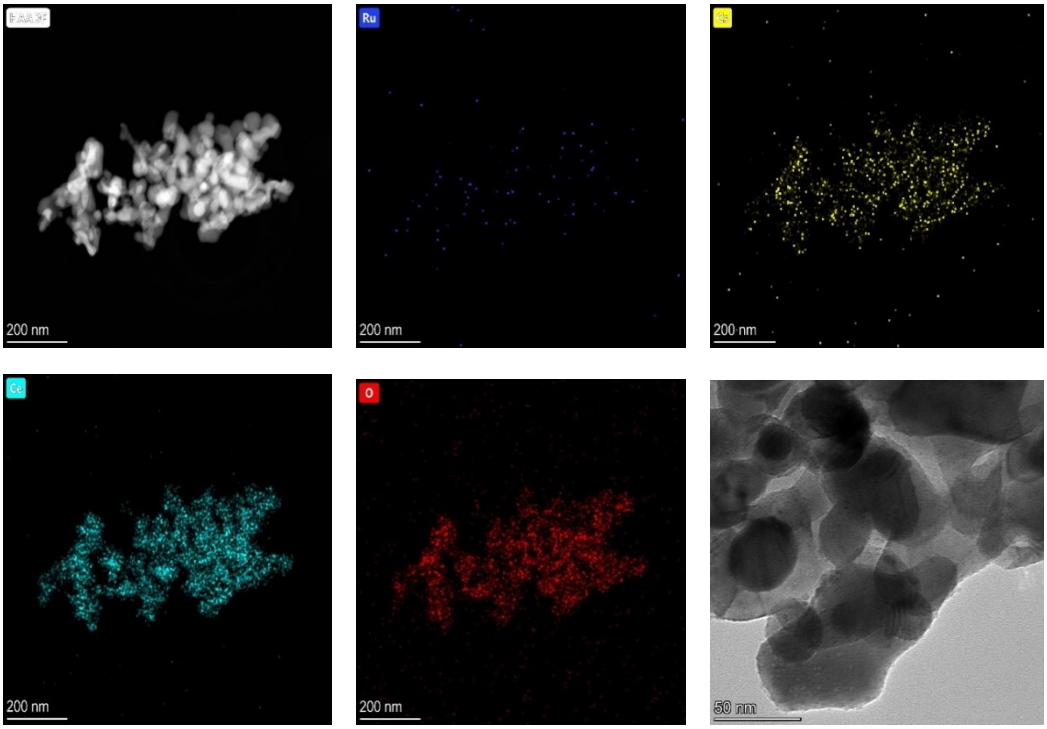


**Fig. S2.** Aaberration-corrected HAADF-STEM images, EDX elemental mappings, and HR-TEM images of Cs-Ru/$CeO_2$.

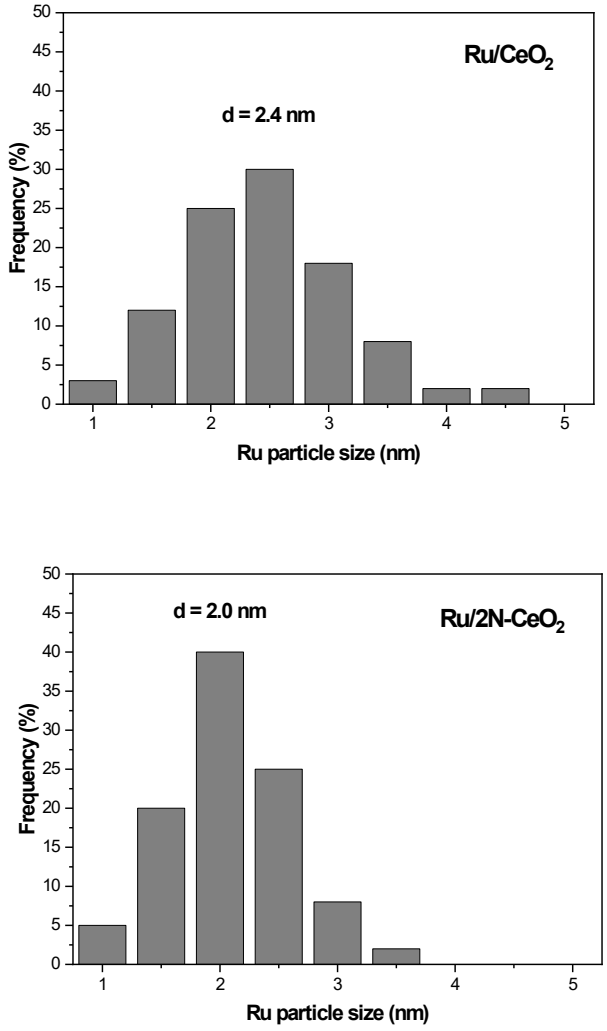


**Fig. S3.** Ru particle size distribution of $Ru/CeO_2$ and $Ru/2N\text{-}CeO_2$ catalysts.

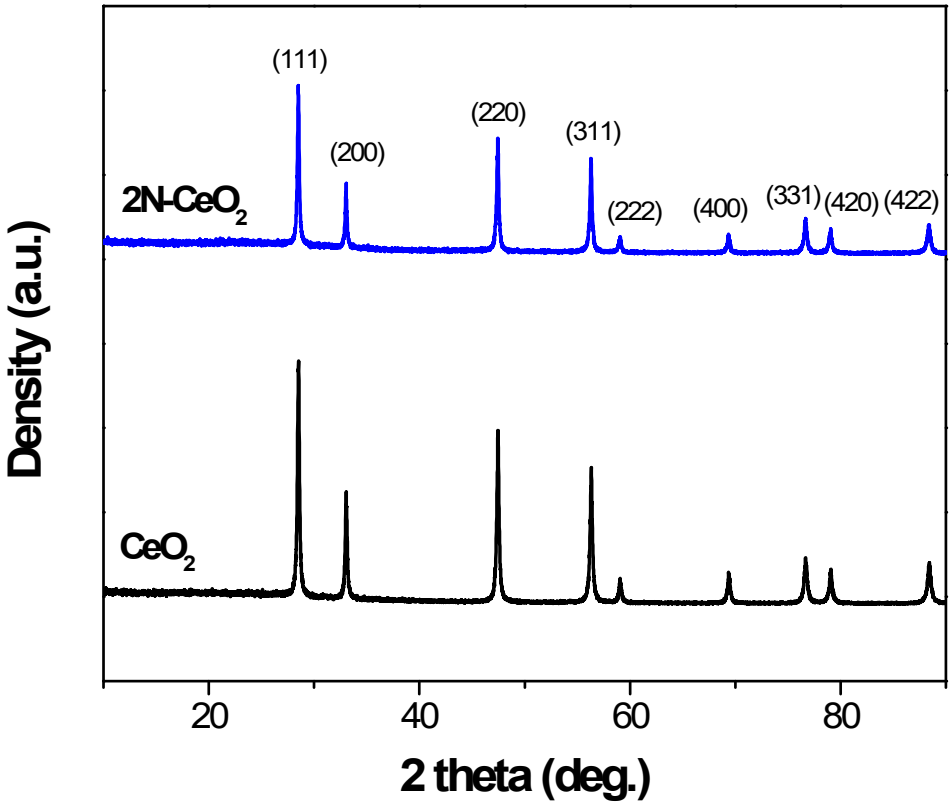


**Fig. S4.** XRD patterns of $CeO_2$ and 2N-$CeO_2$ supports.

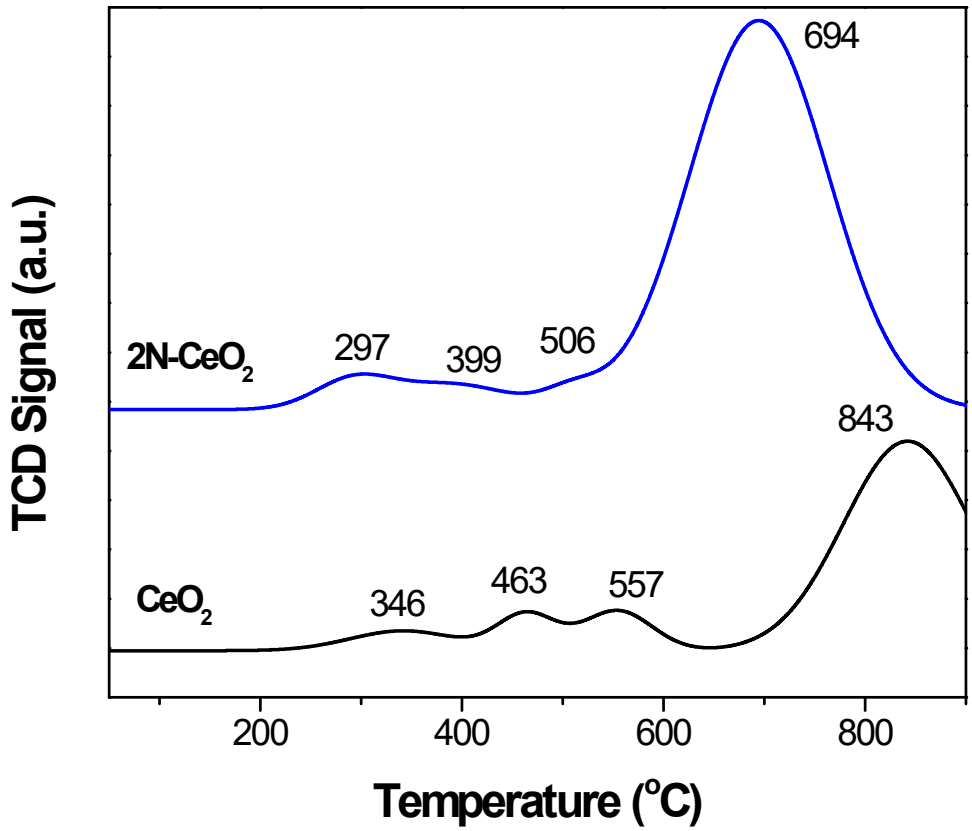


**Fig. S5.** $H_2$-TPR profiles of $CeO_2$ and 2N-$CeO_2$ supports.

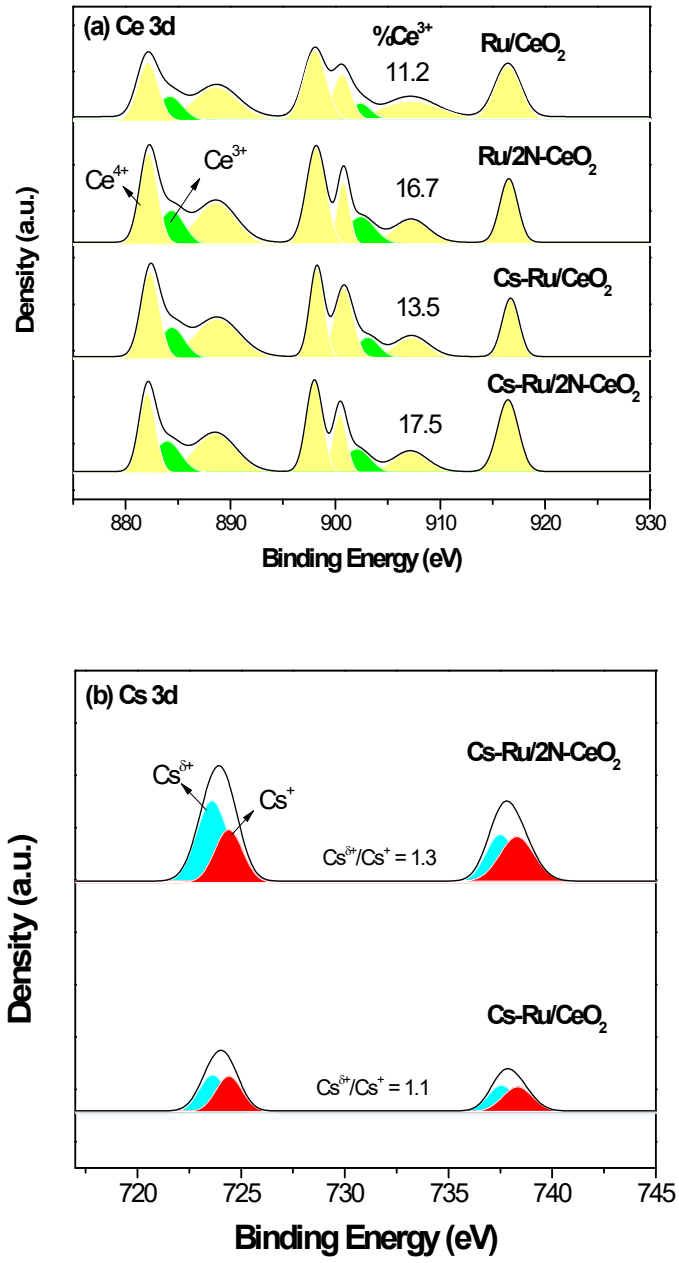


**Fig. S6.** (a) Ce 3d XPS profiles over reduced catalysts, (b) Cs 3d XPS profiles over reduced Cs-Ru/$CeO_2$ and Cs-Ru/2N-$CeO_2$ catalysts.

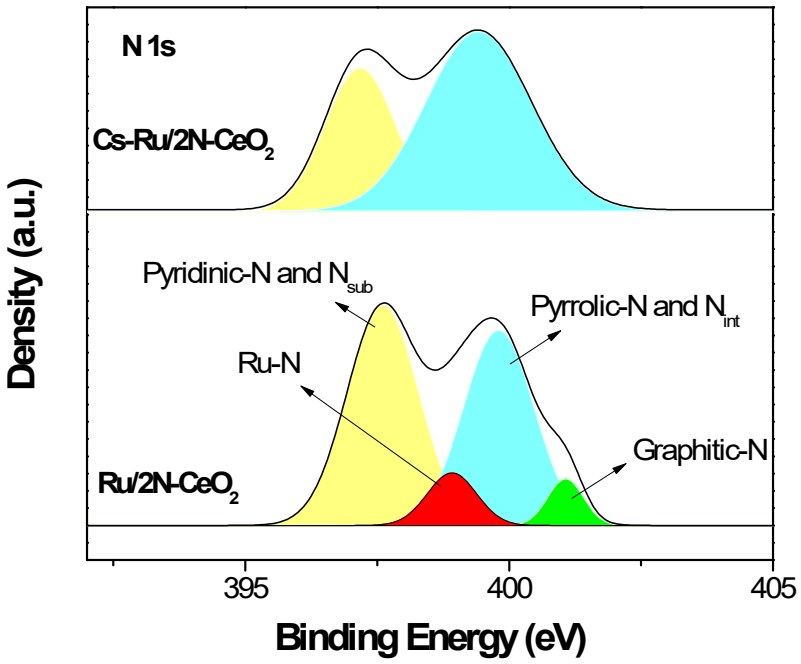


**Fig. S7.** N 1s XPS profiles over reduced Cs-Ru/2N-$CeO_2$ and Ru/2N-$CeO_2$ catalysts.

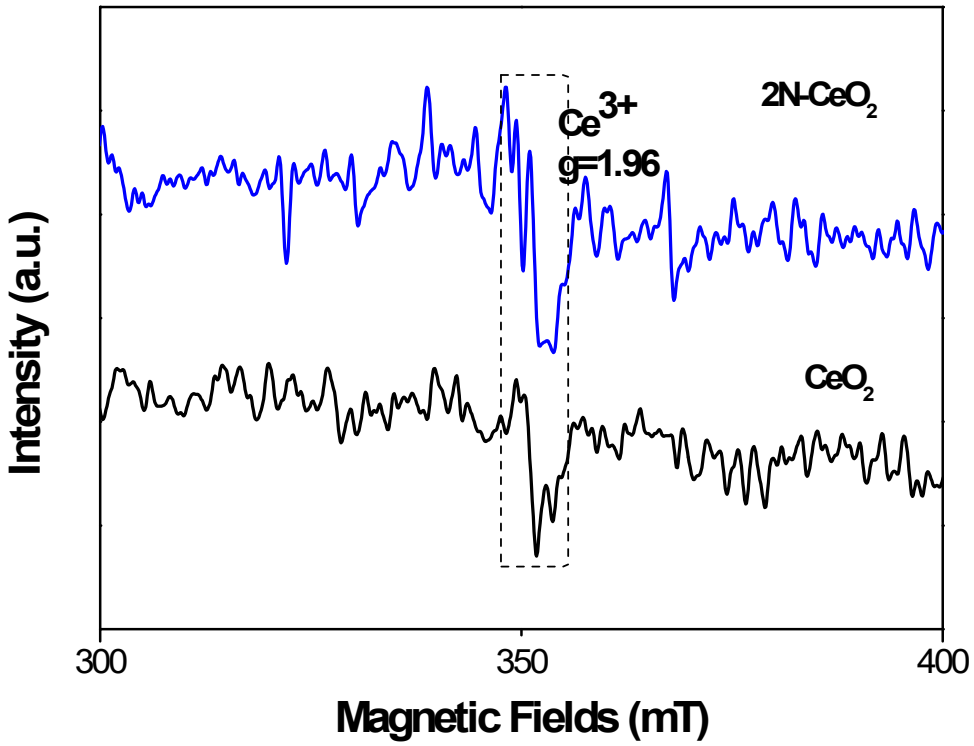


**Fig. S8.** EPR spectra of $CeO_2$ and 2N-$CeO_2$ supports.

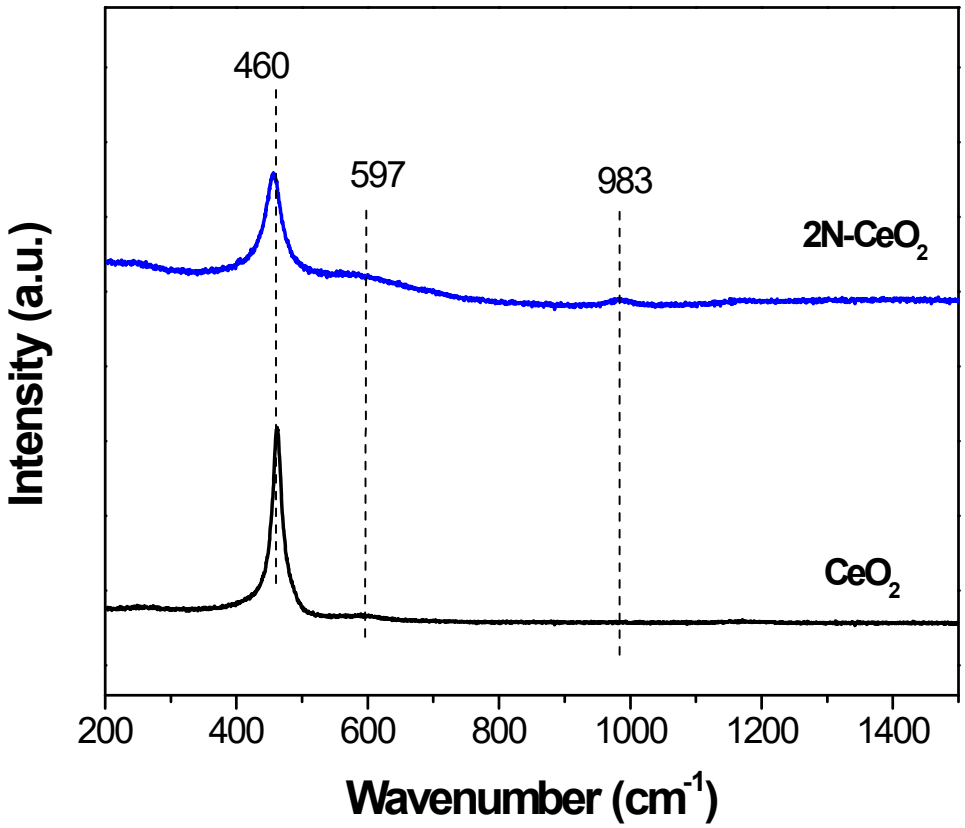


**Fig. S9.** Raman spectra of $CeO_2$ and 2N-$CeO_2$ supports.

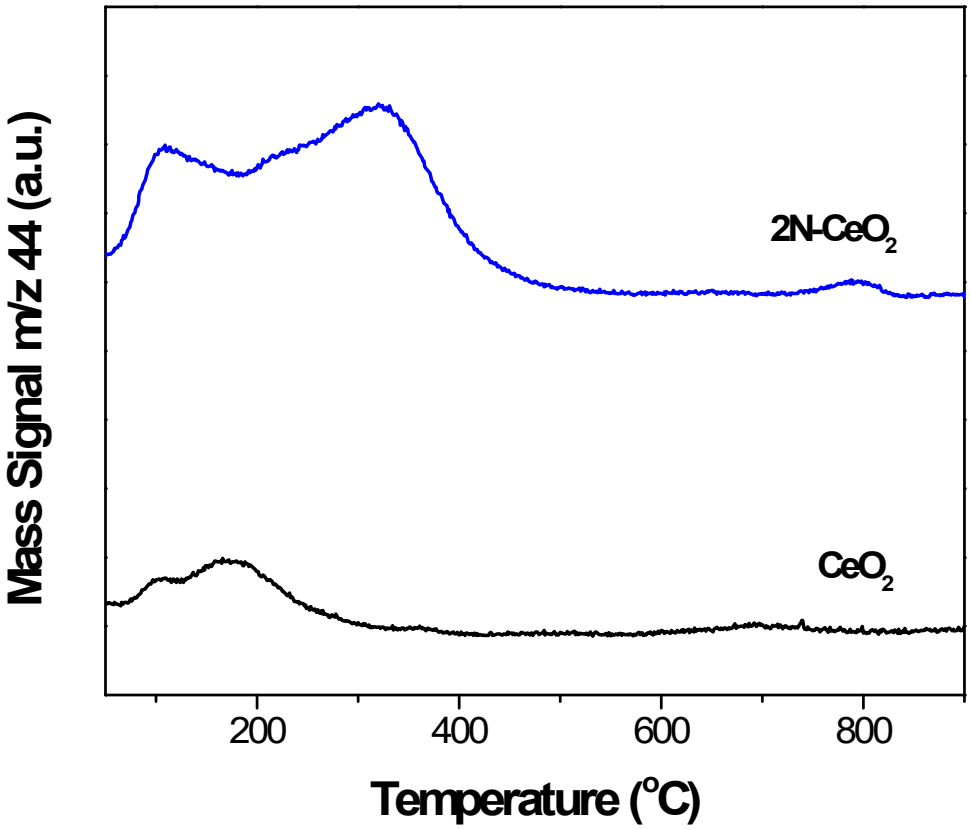


**Fig. S10.** $CO_2$-TPD profiles of $CeO_2$ and 2N-$CeO_2$ supports.

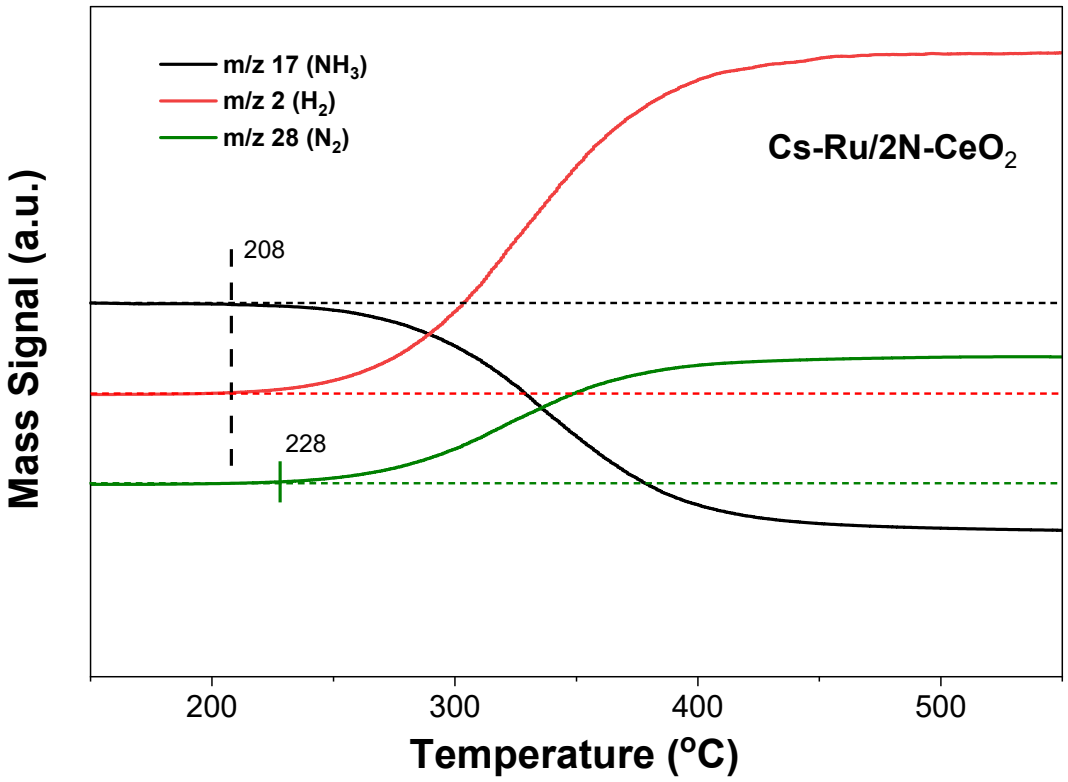


**Fig. S11.** $NH_3$-TPSR of Cs-Ru/2N-$CeO_2$ catalyst.

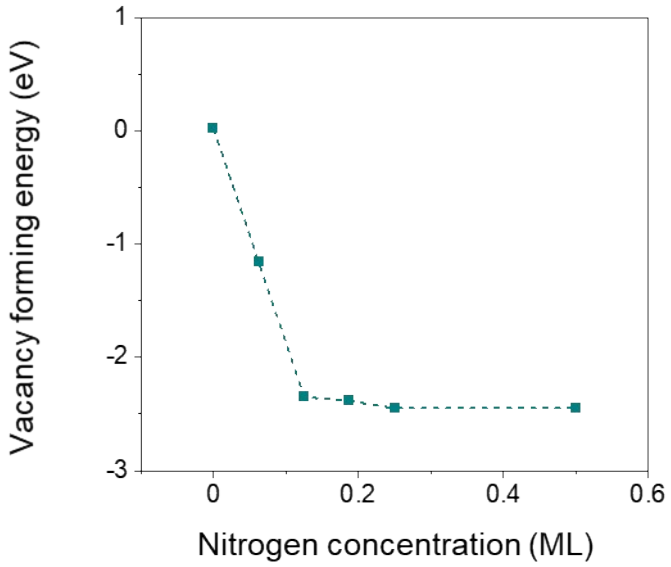


**Fig. S12.** Vacancy forming energies of $CeO_2$ (111) plotted as a function of nitrogen concentration.

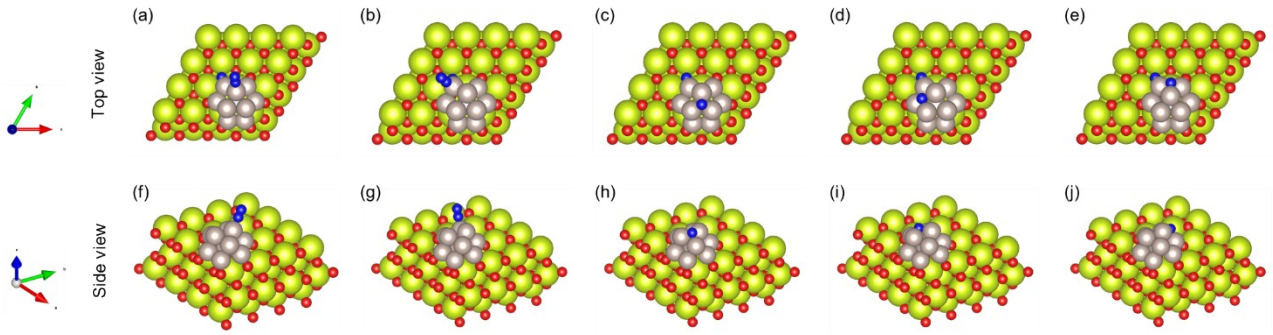


**Fig. S13.** Top and diagonal views of optimized $N_2^*$ and $N^*$ adsorption configurations on $Ru_{10}/N_1$-$CeO_2$ surface.

**Table S1.** The catalytic activity of Ru-based catalysts at 450 °C.

| Catalyst | Ru content (wt%) | WHSV ($mL_{NH_3}/g_{cat.}.h$) | $X_{NH_3}$ (%) | $r_{H_2}$ (mmol/min/$g_{cat.}$) | $r_{H_2}$ (mmol/min/$g_{Ru}$) | $TOF_{H_2}$ ($s^{-1}$) | Ref. |
|---|---|---|---|---|---|---|---|
| **Ru/2N-$CeO_2$** | 1.5 | 30000 | 63.0 | 21.1 | 1406.7 | 4.7 | This work |
| | | 6000 | 97.3 | 6.5 | 433.3 | 1.5 | |
| **Cs-Ru/2N-$CeO_2$** | 1.3 | 30000 | 82.0 | 27.5 | 2115.4 | 15.8 | |
| | | 6000 | 98.9 | 6.6 | 507.7 | 3.8 | |
| **2K-3%Ru/MgO** | 2.7 | 30000 | 83.9 | 28.1 | 1040.7 | 6.5 | [8] |
| **Ru/$MgAl_2O_4$** | 2.2 | 30000 | 61.4 | 20.6 | 936.4 | 3.1 | [9] |
| **Ru/$Ce_5$/$MgAl_{(600)}$** | 2.0 | 30000 | 86.8 | 27.4 | 1370.0 | 3.9 | [10] |
| **Ru/MgO(111)** | 3.1 | 30000 | 100.0 | 33.5 | 1080.6 | 4.9 | [11] |
| **Ru/Ba-$ZrO_2$** | 3.0 | 30000 | 23.6 | 7.9 | 263.3 | 5.2 | [12] |
| **Cs-Ru/Ba-$ZrO_2$** | 3.0 | 30000 | 37.8 | 12.7 | 423.3 | - | [12] |
| **Ru/MgO** | 3.5 | 30000 | 56.5 | 18.9 | 540.0 | 3.0 | [13] |
| **K-Ru/$Mg_2Al$** | 4.6 | 30000 | 42.7 | 14.3 | 310.9 | 1.5 | [14] |
| **Ru/fumed-$SiO_2$** | 5.0 | 30000 | 49.7 | 16.7 | 334.0 | - | [15] |
| **Ru/BHA** | 2.7 | 30000 | 40.0 | 13.8 | 511.1 | 2.9 | [16] |
| **Ru/Rb-Y** | 2.0 | 30000 | 23.0 | 7.7 | 385.0 | 0.8 | [17] |
| **Ru/$Sm_2O_3$** | 2.0 | 30000 | 59.7 | 18.3 | 915.0 | 3.5 | [18] |
| **Ru/$Y_2O_3$** | 2.0 | 30000 | 47.3 | 14.5 | 725.0 | 1.7 | [19] |
| **Ru/CNTs** | 2.0 | 6000 | 85.4 | 5.7 | 285.0 | 2.0 | [20] |
| **Ru/MPC-$ZrO_2$** | 2.0 | 6000 | 15.0 | 1.0 | 50.0 | 0.1 | [21] |
| **Ru/$CaAlO_x$** | 2.5 | 6000 | 72.0 | 4.8 | 192.0 | - | [22] |
| **Ru/$CeO_2$** | 1.8 | 6000 | 91.5 | 6.1 | 338.9 | 1.1 | [23] |

**Table S2.** The N content was determined by Elemental Analysis over xN-$CeO_2$ supports and reduced Ru/xN-$CeO_2$ catalysts.

| Support | N content (at%) | Catalyst | N content (at%) |
|---|---|---|---|
| $CeO_2$ | 0 | Ru/$CeO_2$ | 0 |
| 1N-$CeO_2$ | 2.4 | Ru/1N-$CeO_2$ | 1.0 |
| 2N-$CeO_2$ | 5.6 | Ru/2N-$CeO_2$ | 1.4 |
| 3N-$CeO_2$ | 7.8 | Ru/3N-$CeO_2$ | 1.7 |

**Table S3.** Textural properties of reduced Ru-based catalysts.

| Catalyst | Ru content[a] (wt%) | Cs content[a] (wt%) | N content[b] (at%) | $S_{BET}$[c] ($m^2/g_{cat.}$) | $V_{pore}$[c] ($mL/g_{cat.}$) | $D_{Ru}$[d] (%) | $S_{Ru}$[d] ($m^2/g_{cat.}$) |
|---|---|---|---|---|---|---|---|
| $Ru/CeO_2$ | 1.9 | 0 | 0 | 28 | 0.09 | 28.3 | 1.97 |
| $Ru/2N\text{-}CeO_2$ | 1.5 | 0 | 1.4 | 29 | 0.08 | 50.4 | 2.76 |
| $Cs\text{-}Ru/CeO_2$ | 1.4 | 2.2 | 0 | 21 | 0.07 | 23.7 | 1.21 |
| $Cs\text{-}Ru/2N\text{-}CeO_2$ | 1.3 | 2.2 | 1.1 | 15 | 0.06 | 22.6 | 1.07 |

[a] The Ru and Cs contents were determined by ICP-MS analysis.

[b] The N content was determined by Elemental Analysis.

[c] The specific area ($S_{BET}$) and the total pore volume ($V_{pore}$) were measured by $N_2$ physisorption analysis.

[d] The Ru dispersion and Ru area were calculated from CO pulse chemisorption analysis.

**Table S4.** Nitrogen (N) content and $N_2$ physisorption properties of $CeO_2$ and 2N-$CeO_2$ supports.

| Sample | N content[a] (at%) | $S_{BET}$[b] ($m^2\ g_{cat}^{-1}$) | $V_{pore}$[b] ($cm^3\ g_{cat}^{-1}$) | $d_{pore}$[b] (nm) |
|---|---|---|---|---|
| $CeO_2$ | 0 | 19 | 0.08 | 25 |
| 2N-$CeO_2$ | 5.6 | 15 | 0.05 | 31 |

[a] The N content was determined by Elemental Analysis.

[b] The specific area ($S_{BET}$), the total pore volume ($V_{pore}$), and the pore diameter ($d_{pore}$) were measured by $N_2$ physisorption analysis.

**Table S5.** $H_2$ consumption amount of Ru-based catalysts as determined by $H_2$-TPR analysis.

| Sample | 1st peak | 2nd peak | 3rd peak | $H_2$ consumption ratio |
|---|---|---|---|---|
| $Ru/CeO_2$ | 0.21 (248)* | 0.27 (282) | 0.06 (416) | 0.54 |
| $Ru/2N\text{-}CeO_2$ | 0.49 (298) | 0.14 (346) | 0.20 (368) | 0.83 |
| $Cs\text{-}Ru/CeO_2$ | 0.38 (208) | 0.13 (252) | 0.25 (394) | 0.76 |
| $Cs\text{-}Ru/2N\text{-}CeO_2$ | 0.47 (334) | 0.36 (352) | 0.17 (379) | 1.00 |

*The number in the parentheses indicates the corresponding temperature of the peak.

**Table S6.** XPS and Raman data analysis.

| Catalyst | XPS | | | | | | | | Raman | |
|---|---|---|---|---|---|---|---|---|---|---|
| | Ru 3p | | | Ce 3d | | O 1s | | | $Ru-O-Ce$ | $Defect\ site\ (Ov_)$ |
| | $Ru^0$ (%) | $Ru^{\delta+}$ (%) | $Ru^{\delta+}/Ru^0$ | $Ce^{3+}$ (%) | $Ce^{4+}$ (%) | $O_L$ (%) | $O_V$ (%) | $O_C$ (%) | | |
| $Ru/CeO_2$ | 22.2 | 77.8 | 3.5 | 11.2 | 88.8 | 68.7 | 15.3 | 16.0 | $1.4x10^{-2}$ | $0.6x10^{-2}$ |
| $Ru/2N\text{-}CeO_2$ | 23.0 | 77.0 | 3.3 | 16.7 | 83.3 | 54.5 | 30.5 | 15.0 | $2.1x10^{-2}$ | $1.2x10^{-2}$ |
| $Cs\text{-}Ru/CeO_2$ | 25.0 | 75.0 | 3.0 | 13.5 | 86.5 | 66.1 | 22.2 | 11.7 | $1.2x10^{-2}$ | $0.7x10^{-2}$ |
| $Cs\text{-}Ru/2N\text{-}CeO_2$ | 28.8 | 71.2 | 2.5 | 17.5 | 82.5 | 41.2 | 34.6 | 24.2 | $1.9x10^{-2}$ | $1.4x10^{-2}$ |

**Table S7.** Raman analysis results of $CeO_2$ and 2N-$CeO_2$ supports.

| Sample | $Defect\ sites$ / $O_v$ | $Peroxide\ species$ |
|---|---|---|
| | $I_{597}/I_{460}$ | $I_{983}/I_{460}$ |
| $CeO_2$ | 0.04 | - |
| 2N-$CeO_2$ | 0.20 | 0.11 |

**Table S8.** The percentage of each acid and basic site contribution over the Ru-based catalysts.

| Catalysts | Amount of each acid site [a] (a.u.) | | | | Amount of each basic site [b] (a.u.) | | | |
|---|---|---|---|---|---|---|---|---|
| | Weak | Medium | Strong | Desorbed $NH_3$ ratio | Weak | Medium | Strong | Desorbed $CO_2$ ratio |
| $Ru/CeO_2$ | 0.53 | 0.21 | 0.16 | 0.90 | 0.46 | 0.07 | 0.34 | 0.87 |
| $Ru/2N\text{-}CeO_2$ | 0.56 | 0.34 | 0.10 | 1.00 | 0.32 | 0.47 | 0.14 | 0.93 |
| $Cs\text{-}Ru/CeO_2$ | 0.32 | 0.19 | 0.09 | 0.60 | 0.59 | 0.23 | 0.08 | 0.90 |
| $Cs\text{-}Ru/2N\text{-}CeO_2$ | 0.31 | 0.30 | 0.03 | 0.64 | 0.42 | 0.54 | 0.04 | 1.00 |

[a] The amount of each acid site was determined by $NH_3$-TPD analysis.

[b] The amount of each basic site was determined by $CO_2$-TPD analysis.

**Table S9.** $N_2^*$ and $N^*$ free formation energy over various $Ru_{10}/CeO_2$ and $Ru_{10}/N_1$-$CeO_2$ surfaces. $T$ = 425 ℃ and $P$ = 50 bar.

| Surface | Free formation energy of $N_2^*$ | | Free formation energy of $N^*$ | | |
|---|---|---|---|---|---|
| | Interfacial layer site | External layer site | External layer 3-fold hollow site | Lateral 3-fold hollow site | Lateral 4-fold hollow site |
| $Ru_{10}/CeO_2$ | -0.84 | -1.13 | -0.55 | -0.41 | -0.25 |
| $Ru_{10}/N_1$-$CeO_2$ | -0.57 | -1.19 | -0.56 | -0.37 | -0.41 |

**References**


1. T. A. Le, Y. Kim, H. W. Kim, S.-U. Lee, J.-R. Kim, T.-W. Kim, Y.-J. Lee and H.-J. Chae, *Appl. Catal. B*, 2021, **285**, 119831.
2. G. Kresse and J. Hafner, *Physical Review B*, 1994, **49**, 14251-14269.
3. G. Kresse and J. Furthmüller, *Computational Materials Science*, 1996, **6**, 15-50.
4. J. Wellendorff, K. T. Lundgaard, A. Møgelhøj, V. Petzold, D. D. Landis, J. K. Nørskov, T. Bligaard and K. W. Jacobsen, *Physical Review B*, 2012, **85**, 235149.
5. S. J. Han, J. Chen, H.-G. Park, K.-W. Jun and S. K. Kim, *Chemical Engineering Journal*, 2025, **508**, 161006.
6. R. Urrego-Ortiz, S. Builes and F. Calle-Vallejo, *ChemCatChem*, 2021, **13**, 2508-2516.
7. F. Studt, F. Abild-Pedersen, J. B. Varley and J. K. Nørskov, *Catal. Lett.*, 2013, **143**, 71-73.
8. H. Huang, H. Deng, Y. Ji, D. Li, C. Chen, H. Fang, Y. Luo and L. Jiang, *J, Catal.*, 2025, **450**, 116298.
9. K. D. Kim, J. Kim, B.-S. An, J. H. Shin, Y. Park, U. Jung, K. B. Yi and K. Y. Koo, *Small*, 2025, **21**, 2407338.
10. J. Shin, U. Jung, J. Kim, K. D. Kim, D. Song, Y. Park, B.-S. An and K. Y. Koo, *Appl. Catal. B*, 2024, **340**, 123234.
11. H. Fang, S. Wu, T. Ayvali, J. Zheng, J. Fellowes, P.-L. Ho, K. C. Leung, A. Large, G. Held, R. Kato, K. Suenaga, Y. I. A. Reyes, H. V. Thang, H.-Y. T. Chen and S. C. E. Tsang, *Nat. Commun.*, 2023, **14**, 647.
12. Z. Wang, Y. Qu, X. Shen and Z. Cai, *Int. J. Hydrogen Energy*, 2019, **44**, 7300-7307.
13. X. Ju, L. Liu, P. Yu, J. Guo, X. Zhang, T. He, G. Wu and P. Chen, *Appl. Catal. B*, 2017, **211**, 167-175.
14. Q. Su, L. L. Gu, A. H. Zhong, Y. Yao, W. J. Ji, W. P. Ding and C. T. Au, *Catal. Lett.*, 2018, **148**, 894-903.
15. X.-K. Li, W.-J. Ji, J. Zhao, S.-J. Wang and C.-T. Au, *J, Catal.*, 2005, **236**, 181-189.
16. Z. Wang, Z. Cai and Z. Wei, *ACS Sustainable Chem. Eng.*, 2019, **7**, 8226-8235.
17. J. Cha, T. Lee, Y.-J. Lee, H. Jeong, Y. S. Jo, Y. Kim, S. W. Nam, J. Han, K. B. Lee, C. W. Yoon and H. Sohn, *Appl. Catal. B*, 2021, **283**, 119627.
18. X. Zhang, L. Liu, J. Feng, X. Ju, J. Wang, T. He and P. Chen, *Catal. Sci. Technol.*, 2021, **11**, 2915-2923.
19. J. Feng, L. Liu, X. Ju, J. Wang, X. Zhang, T. He and P. Chen, *ChemCatChem*, 2021, **13**, 1552-1558.
20. C. Chen, Y. Chen, A. M. Ali, W. Luo, J. Wen, L. Zhang and H. Zhang, *Chem. Eng.*

*Technol.*, 2020, **43**, 719-730.

21. Z. Hu, J. Mahin and L. Torrente-Murciano, *Int. J. Hydrogen Energy*, 2019, **44**, 30108-30118.
22. J. Zhao, S. Xu, H. Wu, Z. You, L. Deng and X. Qiu, *Chem. Commun.*, 2019, **55**, 14410-14413.
23. T. A. Le, Y. Kim, S. J. Han, Q. C. Do, G. J. Kim, Y. Im and H.-J. Chae, *Chemical Engineering Journal*, 2024, **493**, 152503.